

ML-CrAIST: Multi-scale Low-high Frequency Information-based Cross black Attention with Image Super-resolving Transformer

Alik Pramanick^[0000–0002–5993–3185], Utsav Bheda^[0009–0008–7636–2610], and
Arijit Sur^[0000–0002–9038–8138]

Indian Institute of Technology Guwahati, India
{p.alik,u.bheda,arijit}@iitg.ac.in

Abstract. Recently, transformers have captured significant interest in the area of single-image super-resolution tasks, demonstrating substantial gains in performance. Current models heavily depend on the network’s extensive ability to extract high-level semantic details from images while overlooking the effective utilization of multi-scale image details and intermediate information within the network. Furthermore, it has been observed that high-frequency areas in images present significant complexity for super-resolution compared to low-frequency areas. This work proposes a transformer-based super-resolution architecture called ML-CrAIST that addresses this gap by utilizing low-high frequency information in multiple scales. Unlike most of the previous work (either spatial or channel), we operate spatial and channel self-attention, which concurrently model pixel interaction from both spatial and channel dimensions, exploiting the inherent correlations across spatial and channel axis. Further, we devise a cross-attention block for super-resolution, which explores the correlations between low and high-frequency information. Quantitative and qualitative assessments indicate that our proposed ML-CrAIST surpasses state-of-the-art super-resolution methods (e.g., 0.15 dB gain @Manga109 $\times 4$). Code is available on <https://github.com/Alik033/ML-CrAIST>.

Keywords: Transformer · Image super-resolution · Spatial domain · Frequency domain · Cross attention

1 Introduction

The task of single image super-resolution (SR) [7] remains an enduring low-level challenge that centers on the restoration of high-resolution (HR) images from degraded low-resolution (LR) inputs. As an issue with inherent ambiguity and numerous possible solutions for a given LR image, several methods have emerged in recent years to address and overcome this challenge. Numerous methods in this context use convolution neural networks (CNNs) [9,10,15,32,35,47] to improve performance in a variety of applications. These methods mostly use residual learning [15], dense connections [35], or channel attention [47] to build

network architectures, significantly contributing to developing super-resolution models. However, the CNN-based approach exhibits a limited receptive field due to the localized nature of convolution, which hampers the global dependencies, consequently restricting the overall performance of the model.

In recent times, the Transformer architecture, initially introduced in natural language processing (NLP), has demonstrated significant success across a wide range of high-level vision tasks [3,4,40]. This success is attributed to its incorporation of a self-attention mechanism, which effectively establishes global dependencies. A notable advancement in SR is SwinIR [20], which presents the Swin Transformer, leading to significant enhancements over state-of-the-art CNN-based models across different standard datasets. Subsequent developments, including Swin-FIR [43], ELAN [45], and HAT [6], have extended the capabilities of SwinIR by utilizing Transformers to develop various network architectures for SR tasks. These methods demonstrate that appropriately enlarging the windows for the shifted window self-attention in SwinIR can lead to obvious improvements in performance. However, the increase in computational burden becomes a significant concern as the window size grows more prominent. Furthermore, Transformer-based methods rely on self-attention and need networks with more channels than previous CNN-based methods [1,14,16]. Also, they use uni-dimensional aggregation operations (either spatial or channel) and homogeneous aggregation schemes (simple hierarchical stacking of convolution and self-attention). Wang et al. [37] consider the above problem and design OmniSR to achieve superior performance. Despite substantial progress in super-resolution methods, they even encounter visual artifacts in the resulting images, such as inadequate texture representation and loss of details. Further, it has been observed that super-resolving high-frequency image areas are more challenging than low-frequency areas. Numerous existing SR methods work solely within the spatial domain, concentrating on improving the resolution of low-resolution pixels to obtain a high-resolution image. They often overlook the potential benefits of the frequency domain, which could offer a better method for retrieving lost high-frequency information. Also, it needs to include more texture patterns of multi-scales, which is required in SR tasks. Similar textures with multiple scales may exist within a single image at different positions. For instance, repetitive patterns at different scales (such as facades, windows, etc., in a building) may appear in various locations within a single image. The multi-scale aware framework is required to use the beneficial non-local detail, which aggregates the information from all the different scales of the LR image.

To address the above mentioned issues and achieve higher performance, this work proposes a novel super-resolution model that simultaneously exploits frequency and spatial domain information at different scales. 2D Discrete Wavelet Transformation (2dDWT) is used to analyze both the high (LH, HL, and HH) and low (LL) frequency wavelet sub-bands. To carefully design a cross-attention block, we fuse low and high frequency information to boost SR performance. We explore the features in multiple scales and systematically combine information across all scales at each resolution level, facilitating meaningful information

exchange. Simultaneously, another fusion technique is proposed to combine the high-frequency sub-bands while maintaining their unique complementary characteristics that differ from simple concatenation or averaging of the sub-bands. The major contributions of this paper are as follows:

1. A novel multi-scale model is proposed by utilizing both spatial and frequency domain features that is capable to enhance the spatial resolution of a low-resolution image.
2. In addition, a low-high frequency interaction block (LHFIB) is introduced to exchange the information between low and high frequency sub-bands through the proposed cross attention block (CAB).
3. A non-linear approach is proposed to fuse high-frequency sub-bands using an attention mechanism for more precise restoration of high-frequency details.
4. Informative features are obtained from different scales using CAB while preserving the high-resolution features to represent spatial details accurately.

2 Related Work

- **Conventional CNNs for SR.** CNNs have achieved remarkable success in the task of image super-resolution. SRCNN [10] is notable as the pioneering CNN-based super-resolution method, outperforming the performance of traditional approaches (e.g., bicubic, nearest-neighbor, and bilinear interpolation). After this initial advancement, significant attention has been directed towards expanding the network depth and incorporating residual learning techniques to enhance super-resolution performance [15,35,47]. EDSR [21] further improves peak signal-to-noise ratio (PSNR) results significantly by removing the unnecessary Batch Normalization layers. Additionally, RCAN [47] integrates a channel attention mechanism to enhance feature aggregation efficiency, enabling improved performance even with deeper network architectures. Subsequent models such as SAN [9], NLSA [28], and HAN [29] have introduced a range of attention mechanisms, either focusing on spatial or channel dimensions, reflecting a growing trend in attention-based approaches within the field. To improve reconstruction quality while working within constrained computing resources, DRCN [16], DRRN [34], CARN [1], IMDN [14] delve into lightweight architectural designs. Another research direction is operating model compression strategies like knowledge distillation [11,46] and neural architecture search [8] to decrease computing costs.
- **Generative adversarial networks (GANs) for SR.** GANs [12] provide a fundamental method to balance perception and distortion by regulating the weights of perceptual and fidelity losses, generating realistic images. [18] introduced SRGAN, which incorporates adversarial training with the SR-ResNet generator. [38] presented ESRGAN featuring the residual-in-residual dense block framework for super-resolution. Later, [33] enhanced ESRGAN by auxiliary noise injection and proposed ESRGAN+. Park et al. [31] suggested Flexible Style SR, which optimizes the SR model with image specific

objectives without viewing the regional features. These methods [18,30,33,38] suffer from the computational burden posed by numerous image maps.

- **Transformer-based methods for SR.** Recently, Transformers have shown significant promise in a range of vision tasks, including image classification [40], object detection [4], semantic segmentation [3], image restoration [5,22,39], etc. Among these approaches, the most prominent example is the Vision Transformer (ViT), demonstrating that transformers can outperform convolutional neural networks in feature encoding tasks. Designing transformer-based models for image super-resolution poses a significant challenge as it requires preserving the structural details of the input image. IPT [5] is a pre-trained model built upon the transformer encoder and decoder structure and has been used for super-resolution. SwinIR [20] employs a window-based attention mechanism to tackle image super-resolution tasks, demonstrating superior performance over CNN-based methods. ELAN [45] facilitates the architecture of SwinIR and utilizes self-attention calculated in different window sizes to capture correlations between long-range pixels. Choi et al. [7] introduce N-gram context into low-level vision tasks using Transformers for the SR task. Most recently, OmniSR [37] explored spatial-channel axis aggregation networks to enhance SR performance.

Our approach also relies on the transformer architecture. Unlike the aforementioned methods, which predominantly utilize spatial domain information and compute self-attention for model construction, our primary focus is on leveraging spatial-frequency domain features and multi-scale features through cross-attention to improve the performance of the super-resolution model.

3 Proposed Method

Figure 1 shows the proposed architecture that aims to generate an SR image from the degraded LR image.

3.1 Overall Pipeline

This section presents a comprehensive description of the overall network architecture. Given an LR image $I_{LR} \in \mathbb{R}^{H \times W \times 3}$, we pass it through a convolution layer to extract the initial feature f_0 . The acquired feature is then fed into N spatial-channel attention-based transformer blocks (SCATB), from which the deep spatial and channel-wise correlated features f_d are extracted.

$$f_0 = \mathcal{C}^{3 \times 3}(I_{LR}), \quad f_i = \mathcal{F}_{SCATB}^i(f^{i-1}), \quad f_d = f_N \quad (1)$$

where $\mathcal{C}^{3 \times 3}$ refers a convolution with 3×3 kernel size, \mathcal{F}_{SCATB}^i represents the i -th SCATB, and f_1, f_2, \dots, f_N denote intermediate features.

Simultaneously, we input I_{LR} into the first low-high frequency interaction block (LHFIB) to extract spatial-frequency information $f_{sf}^1 \in \mathbb{R}^{\frac{H}{2} \times \frac{W}{2} \times c}$ and

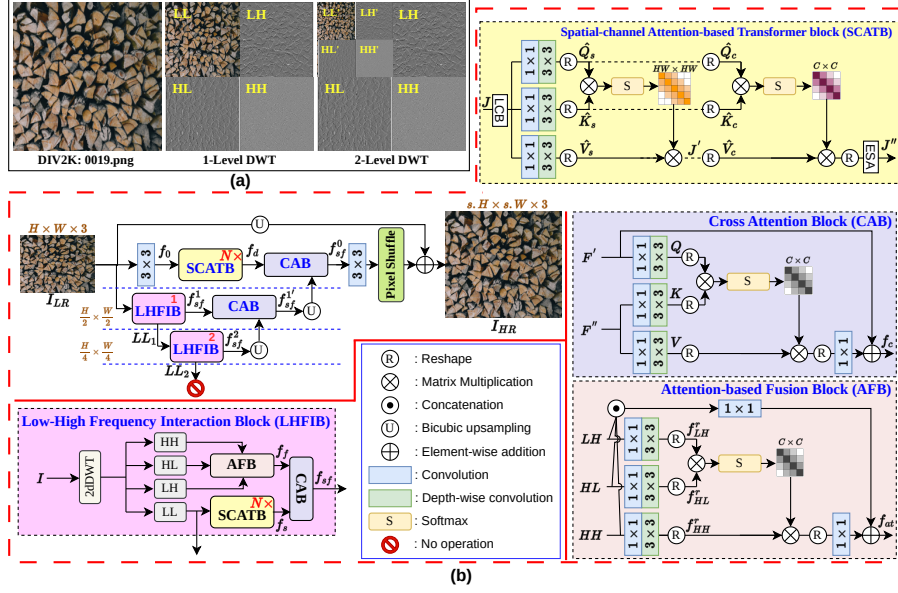


Fig. 1. (a) Multi-level wavelet sub-bands of a LR image. (b) Overview of the Proposed ML-CrAIST. $N \times$ indicates that the block is stacked N times.

LL cube. The LL cube of the first LHFIB is fed into the second LHFIB to extract further spatial-frequency information ($f_{sf}^2 \in \mathbb{R}^{\frac{H}{4} \times \frac{W}{4} \times c}$) in different scales. Each LHFIB contains an attention-based fusion block (AFB) to fuse the high-frequency sub-bands, N number of SCATBs to capture spatially and channel-wise refined features from the low-frequency sub-band, and a cross attention block (CAB) for message passing between refined low-high frequency features. Next, we up-sample f_{sf}^2 and combine it with f_{sf}^1 within the cross-attention block (CAB) to obtain informative multi-scale features, denoted as $f_{sf}^{1'} \in \mathbb{R}^{\frac{H}{2} \times \frac{W}{2} \times c}$. Next, we up-sample the $f_{sf}^{1'}$ feature and fed it alongside f_d into the CAB module to generate meaningful features ($f_{sf}^0 \in \mathbb{R}^{H \times W \times c}$) that contain refined multi-scales feature information.

$$\begin{aligned} f_{sf}^1, LL_1 &= \mathcal{F}_{LHFIB}(I_{LR}), & f_{sf}^2, LL_2 &= \mathcal{F}_{LHFIB}(LL_1), \\ f_{sf}^{1'} &= \mathcal{F}_{CAB}(f_{sf}^1, \mathcal{U}(f_{sf}^2)), & f_{sf}^0 &= \mathcal{F}_{CAB}(f_d, \mathcal{U}(f_{sf}^1)) \end{aligned} \quad (2)$$

where, \mathcal{F}_{LHFIB} , \mathcal{F}_{CAB} , and \mathcal{U} represent the LHFIB, CAB and bicubic up-sampling operation. Next, we employ a convolution layer and set the output channels to $3s^2$, where s denotes the scale factor by which the spatial resolution is to be enhanced. Finally, a PixelShuffle (\mathcal{PS}) layer takes the low-resolution feature maps ($f_l \in \mathbb{R}^{H \times W \times 3s^2}$) and produce the high-resolution image $I_{HR} \in \mathbb{R}^{s.H \times s.W \times 3}$. Then, the reconstructed HR image I_{HR} can be written as

$$I_{HR} = \mathcal{PS}(f_l) + \mathcal{U}(I_{LR}), \quad f_l = C^{3 \times 3}(f_{sf}^0) \quad (3)$$

The proposed ML-CrAIST is optimized using the \mathcal{L}_1 loss:

$$\mathcal{L}_1(I_{HR}^g, I_{HR}) = \frac{1}{M} \sum_{a=1}^M \|(I_{HR})^a - (I_{HR}^g)^a\|_1 \quad (4)$$

where I_{HR}^g indicates the ground-truth image.

3.2 Spatial-channel attention-based transformer block (SCATB)

Wang et al. [37] introduced the omni-self attention (OSA) block, which has been integrated to capture pixel interactions from spatial and channel dimensions simultaneously, enabling the exploration of potential correlations across spatial and channel dimensions. Instead of using a standard transformer block, we leverage the OSA block along with LCB [37] and ESA [17] block as a SCATB to capture useful local details and long-range dependencies effectively.

To formally define its operational principle, let $J \in \mathbb{R}^{H \times W \times C}$ be the intermediate feature map that passes through an LCB block (\mathcal{F}_{LCB}) to aggregate local contextual information (f_c^l), then SCATB generates query (Q), key (K) and value (V) projections by using a 1×1 convolution ($\mathcal{C}^{1 \times 1}$) followed by 3×3 depth-wise convolution ($\mathcal{D}_c^{3 \times 3}$) on f_c^l , where $Q, K, V \in \mathbb{R}^{H \times W \times C}$. Next, we reshaped query ($\hat{Q}_s \in \mathbb{R}^{HW \times C}$), key ($\hat{K}_s \in \mathbb{R}^{C \times HW}$), and value ($\hat{V}_s \in \mathbb{R}^{HW \times C}$) projections, and calculate the attention map of size $\mathbb{R}^{HW \times HW}$ between \hat{Q}_s and \hat{K}_s in spatial dimension which is multiplied with the \hat{V}_s to get the spatially enriched attentive features J' . Next stage, to get the attention map of size $\mathbb{R}^{C \times C}$ in channel dimension, we reshape query ($\hat{Q}_c \in \mathbb{R}^{C \times HW}$), key ($\hat{K}_c \in \mathbb{R}^{HW \times C}$) and J' as value ($\hat{V}_c \in \mathbb{R}^{C \times HW}$). Then, we perform the matrix multiplication between \hat{Q}_c and \hat{K}_c followed by a softmax operation and get the channel-wise attentive feature map. Finally, the channel-wise attentive feature maps are multiplied with the \hat{V}_c and get the spatial and channel-wise correlated feature maps. Lastly, these feature maps are fed into the ESA block (\mathcal{F}_{ESA}) to refine the features further. Overall, the procedure is described as:

$$\begin{aligned} Q, K, V &= \mathcal{D}_c^{3 \times 3}(\mathcal{C}^{1 \times 1}(f_c^l)), \quad f_c^l = \mathcal{F}_{LCB}(J), \quad \hat{K}_s = \mathcal{R}(K), \\ \hat{Q}_s &= \mathcal{R}(Q), \quad \hat{V}_s = \mathcal{R}(V), \quad J' = \mathcal{S}(\hat{K}_s \cdot \hat{Q}_s) \cdot \hat{V}_s, \quad \hat{K}_c = \mathcal{R}(\hat{K}_s), \\ \hat{Q}_c &= \mathcal{R}(\hat{Q}_s), \quad \hat{V}_c = \mathcal{R}(J'), \quad J'' = \mathcal{F}_{SCATB}(J) = \mathcal{F}_{ESA}(\mathcal{S}(\hat{K}_c \cdot \hat{Q}_c) \cdot \hat{V}_c), \end{aligned} \quad (5)$$

where \mathcal{S} , \mathcal{R} , and \mathcal{F}_{SCATB} , indicate the softmax function, reshape, and spatial-channel attention-based transformer operation, respectively. We encourage the reader to refer [37] for more details. We have demonstrated that OSA is advantageous over standard transformer block [41] in producing visually pleasing SR images in the experiments section.

3.3 Low-High Frequency Interaction Block (LHFIB)

In this work, to integrate frequency domain information with spatial domain, we apply the Haar wavelet transformation as a 2D discrete wavelet transformation

to the LR image (I_{LR}) and decompose it into four sub-bands (LL, LH, HL, and HH) where every sub-band $\in \mathbb{R}^{\frac{H}{2} \times \frac{W}{2} \times 1}$. The LL sub-band characterizes the background details within the image, while LH, HL, and HH sub-bands characterize variations along vertical axis, variations along horizontal axis, and diagonal information present in the image. The LL sub-band and the original degraded image are typically employed for analyzing spatial information. Since LH, HL, and HH sub-bands preserve high-frequency components, they provide richer content for enhancing high-frequency detail during the super-resolution process. To leverage the benefit of frequency and spatial details, we design a low-high frequency interaction block.

In detail, let it take I as input and break it down into LL, LH, HL , and HH components. Next, we combine the high-frequency sub-bands (i.e., LH, HL , and HH) using an attention-based fusion block (AFB) and get the refined high-frequency information f_f . The low-frequency (i.e., LL) sub-band is fed into SCATB to extract useful spatial information f_s . Finally, we have performed the cross-attention between low and high-frequency features to enable intelligent feature aggregation. The entire approach can be formulated as:

$$\begin{aligned} LL, LH, HL, HH &= \mathcal{F}_{DWT}(I), \quad f_f = \mathcal{F}_{AFB}(LH, HL, HH), \\ f_s &= \mathcal{F}_{SCATB}(LL), \quad f_{sf} = \mathcal{F}_{CAB}(f_f, f_s), \quad f_{sf}, LL = \mathcal{F}_{LHFIB}(I) \end{aligned} \quad (6)$$

where \mathcal{F}_{DWT} , \mathcal{F}_{AFB} , \mathcal{F}_{CAB} and \mathcal{F}_{LHFIB} refer 2dDWT, attention-based fusion, cross-attention, and low-high frequency interaction operation, respectively.

3.4 Attention-based fusion block (AFB)

The conventional method for feature aggregation typically involves either simple concatenation or summation. However, these types of selection offer restricted expressive capabilities of the network, as [19] suggested. In this context, we present a nonlinear method for merging features through an attention mechanism to identify and amplify the more relevant features. As shown in Figure 1, we propose an attention-based fusion block (AFB) to combine the high-frequency cubes so that only useful information can be processed further. We pass the high-frequency sub-bands through a convolution layer with 1×1 kernel size and a depth-wise convolution layer with 3×3 kernel size. Next, we reshape the features to obtain $f_{LL}^r, f_{HH}^r \in \mathbb{R}^{C \times HW}$ and $f_{HL}^r \in \mathbb{R}^{HW \times C}$. We compute the matrix multiplication between f_{LH}^r and f_{HL}^r followed by a softmax operation to get the attentive map (f_a) of size $\mathbb{R}^{C \times C}$. This attention map f_a is multiplied with f_{HH}^r to obtain attentive feature f_{at} . Finally, the concatenated LH, HL, and HH sub-bands are convolved through a 1×1 convolution and added with the reshaped attentive feature to produce the attention-based fused high-frequency features. Such an operation can be defined as:

$$\begin{aligned} f_{sb} &= \mathcal{D}_c^{3 \times 3}(\mathcal{C}^{1 \times 1}(sb)), \quad f_{sb}^r = \mathcal{R}(f_{sb}), \quad sb \in \{LH, HL, HH\} \\ f_{at} &= \mathcal{F}_{AFB}(LH, HL, HH) = \mathcal{C}^{1 \times 1}(LH \odot HL \odot HH) \\ &\quad + \mathcal{C}^{1 \times 1}(\mathcal{R}(\mathcal{S}(f_{LH}^r \cdot f_{HL}^r) \cdot f_{HH}^r)), \end{aligned} \quad (7)$$

where \mathcal{S} , \mathcal{R} , \odot refer to softmax function, reshape operation, and concatenation operation, respectively. Through ablation, we have shown that the AFB yields more promising outcomes than regular concatenation and addition.

3.5 Cross Attention Block (CAB)

CAB integrates two distinct embedding sequences of identical dimensions. It employs query from one sequence and key and value from the other. The attention masks from one embedding sequence are used to emphasize the extracted features in another embedding sequence. We introduce two cross-attention blocks (CAB) with similar architectures for message passing: one operates between low-high frequency features, and the other operates between multi-scale features. For low-high frequency features, it leverages the low frequency features (F') to generate a query projection and employs high frequency features (F'') to create key and value projections through a standard 1×1 convolution and a 3×3 depth-wise convolution layer. Similarly, in the multi-scale scenario, one scale feature (F') is used to generate the query projection, while another scale feature (F'') is used to create the key and value projections. Overall, cross-attention can be obtained by

$$\begin{aligned} Q &= \mathcal{D}_c^{3 \times 3}(\mathcal{C}^{1 \times 1}(F')), \quad K, V = \mathcal{D}_c^{3 \times 3}(\mathcal{C}^{1 \times 1}(F'')), \quad Q_r = \mathcal{R}(Q), \\ K_r &= \mathcal{R}(K), \quad V_r = \mathcal{R}(V), \quad \mathcal{CA}(Q_r, K_r, V_r) = \mathcal{S}(Q_r \cdot K_r) \cdot V_r, \\ f_c &= \mathcal{F}_{\text{CAB}}(Q, K, V) = \mathcal{C}^{1 \times 1}(\mathcal{R}(\mathcal{CA}(Q_r, K_r, V_r))) + F', \end{aligned} \quad (8)$$

where $Q, V \in \mathbb{R}^{C \times HW}$, $K \in \mathbb{R}^{HW \times C}$, and \mathcal{CA} represents the cross-attention function.

4 Experiments

4.1 Datasets & Evaluation Metrics

Following prior research [20,7,37], we employ the DIV2K dataset [36] for training. For testing purposes, we utilize five widely recognized benchmark datasets: Set5 [2], Set14 [42], B100 [26], Urban100 [13], and Manga109 [27]. The testing results are assessed based on PSNR and structural similarity index measure (SSIM) values computed on the Y channel (i.e., luminance) within the YCbCr color space. Also, we evaluate the learned perceptual image patch similarity (LPIPS) metrics. It measures how similar two images appear to the human visual system.

4.2 Implementation Details

We augment the data during training by applying random horizontal flips and 90/180/270-degree rotations. For a fair comparison with the existing works, LR images are obtained through bi-cubic down-sampling from HR images. Empirically, the number of SCATBs in ML-CrAIST is set to 5. Also, the attention head

number is set to 4, and the window size is set to 8. We train the model using the Adam optimizer with a batch size of 32 for 1000K iterations, starting with an initial learning rate of 10^{-4} , which is decreased by half after every 200k iterations. During each training iteration, LR patches of size 64×64 are randomly cropped as input. We have set the number of channels 64 in each convolution layer for ML-CrAIST (Ours). The proposed work is implemented using PyTorch, and all experimentations are performed on a single NVIDIA V100 GPU. Figure 5(b) shows the convergence of the model that we observed.

In our lighter version of ML-CrAIST (Ours-Li), we have used the same architecture shown in Figure 1 with a reduced number of channels in each convolution layer from 64 to 48.

Method	Years	#params (K)	FLOPs		Set5		Set14		B100		Urban100		Manga109	
			(K)	(G)	PSNR	SSIM	PSNR	SSIM	PSNR	SSIM	PSNR	SSIM	PSNR	SSIM
VDSR	CVPR'16	666	613	36.66	0.9542	33.05	0.9127	31.90	0.8960	30.76	0.9140	37.22	0.9750	
MemNet	ICCV'17	678	2662.4	37.78	0.9597	33.28	0.9142	32.08	0.8978	31.31	0.9195	37.72	0.9740	
SRMDNF	CVPR'18	1511	-	37.79	0.960	33.32	0.915	32.05	0.8985	31.33	0.9204	38.07	0.9761	
CARN	ECCV'18	1592	222.8	37.76	0.9590	33.52	0.9166	32.09	0.8978	31.92	0.9256	38.36	0.9765	
IMDN	MM'19	694	158.8	38.00	0.9605	33.63	0.9177	32.19	0.8996	32.17	0.9283	38.88	0.9774	
LatticeNet	2x ECCV'20	756	169.5	38.06	0.9610	33.78	0.9193	32.25	0.9005	32.43	0.9302	38.94	0.9774	
SwinIR	ICCV'21	878	195.6	38.14	0.9611	33.86	0.9206	32.31	0.9012	32.76	0.9340	39.12	0.9783	
ESRT	CVPRW'22	677	191.4	38.03	0.9600	33.75	0.9184	32.25	0.9001	32.58	0.9318	39.12	0.9774	
NGSwin	CVPR'23	998	140.4	38.05	0.9610	33.79	0.9199	32.27	0.9008	32.53	0.9324	38.97	0.9777	
OmniSR	CVPR'23	772	147.2	38.22	0.9613	33.98	0.9210	32.36	0.9020	33.05	0.9363	39.28	0.9784	
Ours-Li		743	97.2	38.15	0.9615	33.64	0.9213	32.35	0.9020	32.93	0.9361	39.23	0.9785	
Ours		1259	165.7	38.19	0.9617	33.77	0.9220	32.36	0.9022	33.04	0.9370	39.26	0.9786	
VDSR	CVPR'16	666	613	33.66	0.9213	29.77	0.8314	28.82	0.7976	27.14	0.8279	32.01	0.9340	
MemNet	ICCV'17	678	2662.4	34.09	0.9248	30.00	0.8350	28.96	0.8001	27.56	0.8376	32.51	0.9369	
EDSR	CVPRW'17	1555	160.2	34.37	0.9270	30.28	0.8417	29.09	0.8052	28.15	0.8527	33.45	0.9439	
SRMDNF	CVPR'18	1528	-	34.12	0.9254	30.04	0.8382	28.97	0.8025	27.57	0.8398	33.00	0.9403	
CARN	ECCV'18	1592	118.8	34.29	0.9255	30.29	0.8407	29.06	0.8034	28.06	0.8493	33.50	0.9440	
IMDN	MM'19	703	56.3	34.36	0.9270	30.32	0.8417	29.09	0.8046	28.17	0.8519	33.61	0.9445	
RFDN-L	ECCV'20	633	65.6	34.47	0.9280	30.35	0.8421	29.11	0.8053	28.32	0.8547	33.78	0.9458	
LatticeNet	3x ECCV'20	765	76.3	34.40	0.9272	30.32	0.8416	29.10	0.8049	28.19	0.8513	33.63	0.9442	
SwinIR	ICCV'21	886	87.2	34.62	0.9289	30.54	0.8463	29.20	0.8082	28.66	0.8624	33.98	0.9478	
ESRT	CVPRW'22	770	96.4	34.42	0.9268	30.43	0.8433	29.15	0.8063	28.46	0.8574	33.95	0.9455	
NGSwin	CVPR'23	1007	66.6	34.52	0.9282	30.53	0.8456	29.19	0.8078	28.52	0.8603	33.89	0.9470	
OmniSR	CVPR'23	780	74.4	34.70	0.9294	30.57	0.8469	29.28	0.8094	28.84	0.8656	34.22	0.9487	
Ours-Li		749	49.6	34.58	0.9294	30.23	0.8474	29.28	0.8106	28.73	0.8651	34.26	0.9492	
Ours		1268	84.1	34.70	0.9302	30.39	0.8488	29.31	0.8111	28.89	0.8676	34.42	0.9501	
VDSR	CVPR'16	666	613	31.35	0.8838	28.01	0.7674	27.29	0.7251	25.18	0.7524	28.83	0.8870	
MemNet	ICCV'17	678	2662.4	31.74	0.8893	28.26	0.7723	27.40	0.7281	25.50	0.7630	29.42	0.8942	
EDSR	CVPRW'17	1518	114.0	32.09	0.8938	28.58	0.7813	27.57	0.7357	26.04	0.7849	30.35	0.9067	
SRMDNF	CVPR'18	1552	-	31.96	0.8925	28.35	0.7787	27.49	0.7337	25.68	0.7731	30.09	0.9024	
CARN	ECCV'18	1592	90.9	32.13	0.8937	28.60	0.7806	27.58	0.7349	26.07	0.7837	30.47	0.9084	
IMDN	MM'19	715	40.9	32.21	0.8948	28.58	0.7811	27.56	0.7353	26.04	0.7838	30.45	0.9075	
RFDN-L	ECCV'20	643	37.4	32.28	0.8957	28.61	0.7818	27.58	0.7363	26.20	0.7883	30.61	0.9096	
LatticeNet	4x ECCV'20	777	43.6	32.30	0.8962	28.68	0.7830	27.62	0.7367	26.25	0.7873	30.54	0.9075	
SwinIR	ICCV'21	897	49.6	32.44	0.8976	28.77	0.7858	27.69	0.7406	26.47	0.7980	30.92	0.9151	
ESRT	CVPRW'22	751	67.7	32.19	0.8947	28.69	0.7833	27.69	0.7379	26.39	0.7962	30.75	0.9100	
NGSwin	CVPR'23	1019	36.4	32.33	0.8963	28.78	0.7859	27.66	0.7396	26.45	0.7963	30.80	0.9128	
OmniSR	CVPR'23	792	37.8	32.49	0.8988	28.78	0.7859	27.71	0.7415	26.64	0.8018	31.02	0.9151	
Ours-Li		758	25.5	32.15	0.8962	28.40	0.7863	27.73	0.7426	26.53	0.8019	31.11	0.9162	
Ours		1280	42.9	32.36	0.8984	28.53	0.7895	27.78	0.7446	26.68	0.8057	31.17	0.9176	

Table 1. PSNR and SSIM comparison with the state-of-the-art on five datasets. Best, second best, and third best performance are presented in red, blue, and green.

4.3 Comparisons with the SOTA

To validate the superiority of ML-CrAIST, we compare it against recent state-of-the-art methods (SOATs) under a scale factor of 2, 3, and 4, respectively. In particular, former works, VDSR [15], MemNet [35], EDSR [21], SRMDNF [44], CARN [1], IMDN [14], RFDN-L [23], LatticeNet [25], SwinIR [20], ESRT [24], NGSwin [7], and OmniSR [37] are introduced for comparison.

■ **Quantitative results.** The quantitative results are presented in Table 1.

In order to be fair comparison throughout the evaluation process, all models

undergo training and testing processes using the same dataset. It is clear from the results that our method achieves the highest performance across all testing datasets. Compared to [37], ML-CrAIST has 0.20 dB improvement on Manga109 ($\times 3$). Also, we noticed that our method demonstrates the most significant improvement on B100, Urban100, and Manga109 datasets compared to existing methods, indicating its suitability for images rich in textured regions, geometric structures, and finer details of SR images. As shown in Table 2, we obtain a lower LPIPS score, suggesting a higher perceptual quality of the SR image. It is worth noting that by incorporating the frequency details and analyzing the features in multiple scales, ML-CrAIST surpasses the performance of the existing methods. Additionally, in Table 1, we have shown the results of our lighter method (**Ours-Li**) with reduced parameters and FLOPs. It takes the minimum FLOPs among all the existing schemes with comparable results. The FLOPs are $\sim 1.5\times$ lesser than NGSwIn with 1.01% and 0.37% PSNR and SSIM gain on Manga109 ($4\times$). Further, We have shown the computational overhead during inference in Table 3.

Model	Set5	Set14	B100	Urban100	Manga109
IMDN	0.1317 \pm 0.0659	0.1242 \pm 0.0866	0.1907 \pm 0.0601	0.0131 \pm 0.0124	0.0038 \pm 0.0032
SwinIR	0.1287 \pm 0.0642	0.1209 \pm 0.0870	0.1857 \pm 0.0596	0.0111 \pm 0.0106	0.0033 \pm 0.0026
NGSwIn	0.1291 \pm 0.0640	0.1210 \pm 0.0869	0.1861 \pm 0.0595	0.0109 \pm 0.0101	0.0035 \pm 0.0029
OmniSR	0.1293 \pm 0.0641	0.1193 \pm 0.0848	0.1829 \pm 0.0595	0.0102 \pm 0.0093	0.0034 \pm 0.0029
Ours-Li	0.1354 \pm 0.0651	0.1197 \pm 0.0859	0.1842 \pm 0.0595	0.0105 \pm 0.0097	0.0033 \pm 0.0028
Ours	0.1312 \pm 0.0642	0.1173 \pm 0.0845	0.1812 \pm 0.0591	0.0101 \pm 0.0094	0.0032 \pm 0.0027

Table 2. LPIPS score Comparison on $4\times$. Best performance is presented in red. Lower score is better.

scale	Input dimension	Output dimension	Inference time (second)		
			OmniSR	Ours-Li	Ours
$2\times$	(512, 382)	(1024, 764)	4.98	4.24	5.99
$3\times$	(341, 254)	(1023, 762)	2.73	2.12	3.35
$4\times$	(256, 191)	(1024, 764)	2.05	1.94	2.61

Table 3. Single image inference time for $2\times$, $3\times$, and $4\times$, respectively

- **Visual Comparison.** Figure 2 shows the visual comparison of our method with SOTAs at $\times 2$, $\times 3$, and $\times 4$ scales. It is observable that the HR images generated by ML-CrAIST exhibit more fine-grained details, whereas other methods produce blurred edges or artifacts in complex regions. For example, in the third image of Figure 2, our model can pleasantly restore the precise texture of the road. The visual results demonstrate that incorporating frequency information and analyzing features across multiple scales enables us to capture more structural information, preserve the geometric structure of the image, and generate realistic HR results.

4.4 Ablation Study

In this subsection, we perform a set of experimentations to exhibit the efficacy of ML-CrAIST in different settings.

- **Number of SCATBs.** Experimentally, we have set the number of SCATBs to 5. We also analyze the model performance by varying the SCATB number

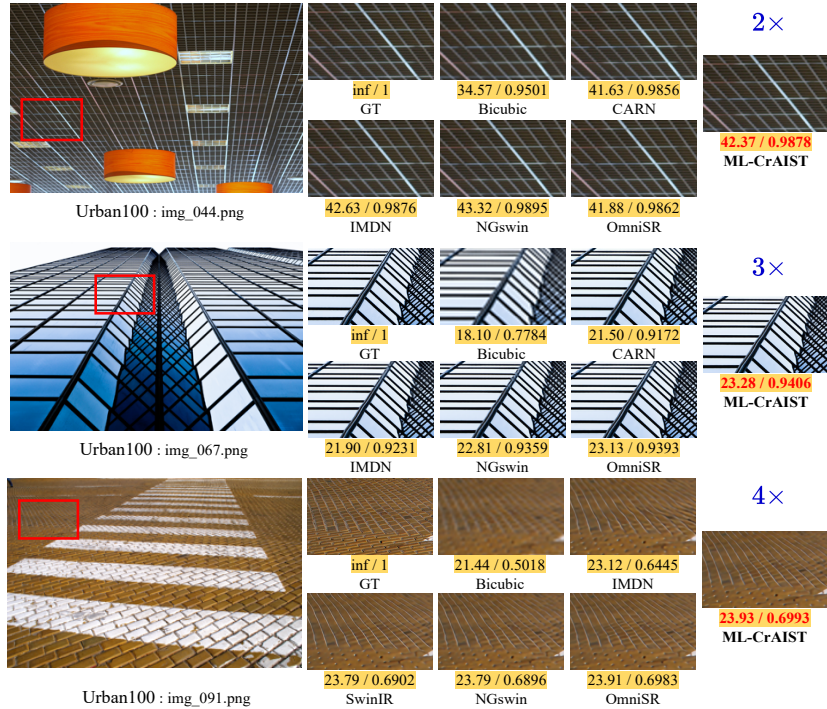


Fig. 2. Visual Comparison of our ML-CrAIST with the SOTA.

N. As depicted in Figure 4, compared to the smallest number of SCATB, increasing the number of SCATB leads to performance gains. It can be seen that ML-CrAIST with $N = 6$ or 7 produces a similar kind of result as $N = 5$ with higher parameters (refer to 4(d)).

- Effect of LHFIB.** We remove the frequency information and only take the spatial information to train our model. Figure 3(a) and 3(b) represent the diagram with and without the frequency information, respectively. The results are reported in the 5th row of the Table 4. The results of ML-CrAIST are superior with the frequency information, displaying that the frequency details can offer global dependency to enhance the representation capability of the model.

Model	FLOPs (G)	Set5		Set14		B100		Urban100		Manga109	
		PSNR	SSIM	PSNR	SSIM	PSNR	SSIM	PSNR	SSIM	PSNR	SSIM
w/o AFB (Addition)	42.80	32.28	0.8974	28.47	0.7886	27.56	0.7431	26.64	0.8041	31.14	0.9174
w/o AFB (Concatenation)	42.82	32.29	0.8974	28.45	0.7885	27.68	0.7435	26.63	0.8056	31.09	0.9174
DWT Level-1	41.11	32.15	0.8957	28.46	0.7872	27.72	0.7423	26.58	0.8022	31.04	0.9157
w/o CAB	41.79	32.31	0.8977	28.52	0.7881	27.76	0.7433	26.65	0.8043	31.10	0.9175
w/o LHFIB	42.53	32.29	0.8975	28.42	0.7888	27.26	0.7434	26.66	0.8050	31.11	0.9164
Full Model	42.91	32.36	0.8984	28.53	0.7895	27.78	0.7446	26.68	0.8057	31.17	0.9176

Table 4. Ablation studies with different settings of our model on 4x. Best result is represented in red.

- Effect of CAB.** We execute experiments to investigate the significance of the CAB. Specifically, we compare the results of the model with and without

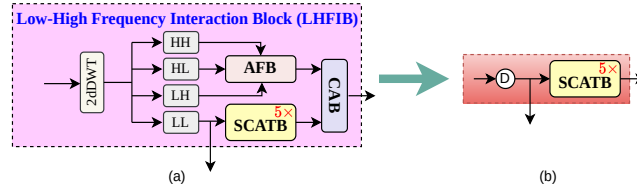


Fig. 3. (a) indicates the LHFIB, (b) indicates the diagram without frequency information. \textcircled{D} indicates the bi-cubic down-sampling operation.

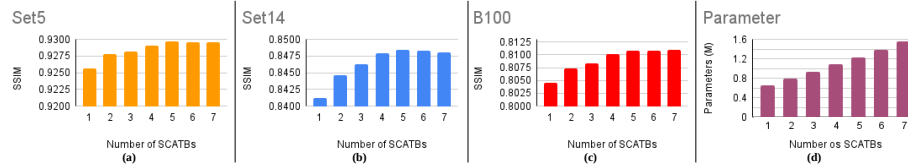


Fig. 4. (a), (b), and (c) refer the SSIM comparison, and (d) refers the number of parameters on $3\times$ with different number of SCATBs.

CAB in the 4th row of Table 4. While removing the CAB, we used a simple element-wise addition operation. From the aspects of quantitative metrics, the use of CAB can obviously improve the SSIM and PSNR performance of the model. The visual comparison is shown in Figure 5(a).

- **Effect of AFB.** We explore the feature aggregation process in the 1st and 2nd row of Table 4. The results demonstrate that the proposed AFB produces promising outcomes compared to summation and concatenation methods.
- **Effect of multi-scale or multi-level DWT.** Third row of Table 4 justifies the importance of the 2-level 2dDWT or multi-scale analysis in our model.

Further, to validate each component of ML-CrAIST, in Figure 6, we have shown results in three different measurements: LPIPS, Blind/Referenceless Image Spatial Quality Evaluator (BRISQUE), and Edge Preservation Index (EPI). It can be seen that the full model has a lower LPIPS and BRISQUE and a high EPI value, which indicates that the image has fewer distortions, artifacts, and better edge preservation, aligns more closely with natural scene statistics, and is visually pleasing to human observers.



Fig. 5. (a) Visual comparison of different settings of ML-CrAIST. (b) Convergence graph of ML-CrAIST.

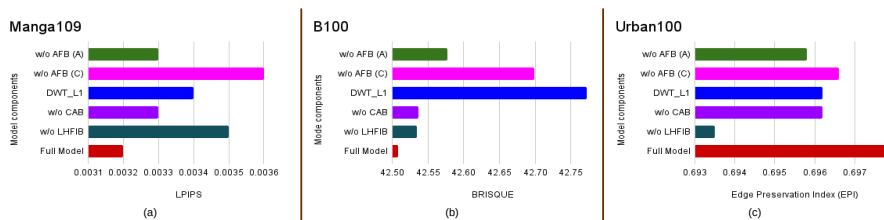


Fig. 6. LPIPS (\downarrow), BRISQUE (\downarrow), and EPI comparison between different components of ML-CrAIST. \downarrow indicates lower is better.

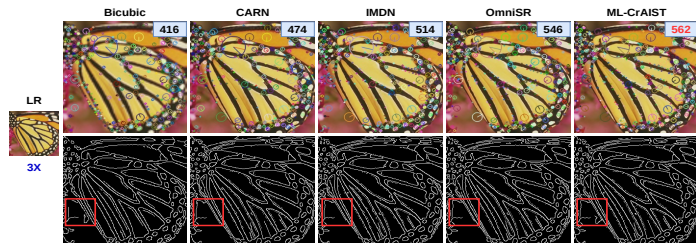


Fig. 7. Key-point and canny edge detection comparison between existing methods and ML-CrAIST. The top corner of the first row indicates the number of key points.

4.5 Impact on various application

To validate the practical applicability of our model, we employ ML-CrAIST as a preprocessing technique for image key-point detection and edge detection tasks, as shown in Figure 7. Initially, we employ scale-invariant feature transform (SIFT) to compute the key points. It can be observed that the key-point detection significantly increases after super-resolving the images using our method. Subsequently, we employ Canny edge detection to identify edges in the super-resolved images. Compared to the super-resolved image by SOTA models, our super-resolved image exhibits more localized edge features. In the second row of Figure 7, we have marked using a red box where our method captures edges perfectly, but others fail.

5 Conclusion

In this paper, we propose a transformer-based multi-scale super-resolution architecture called ML-CrAIST, demonstrating the advantage of modeling both spatial and frequency details for the SR task. Our cross-attention block seamlessly performs message passing between low and high-frequency features across multiple scales in the network and acknowledges their correlation. Furthermore, we propose AFB to effectively fuse the high frequency cubes, which boosts the overall performance. Finally, we validate the rationale and efficiency of the ML-CrAIST by conducting extensive experimentation across various benchmark datasets. We additionally conduct an ablation study to assess the impact of various configurations within ML-CrAIST.

References

1. Ahn, N., Kang, B., Sohn, K.A.: Fast, accurate, and lightweight super-resolution with cascading residual network. In: Proceedings of the European conference on computer vision (ECCV). pp. 252–268 (2018)
2. Bevilacqua, M., Roumy, A., Guillemot, C., Alberi-Morel, M.L.: Low-complexity single-image super-resolution based on nonnegative neighbor embedding. *BMVC* (2012)
3. Cao, H., Wang, Y., Chen, J., Jiang, D., Zhang, X., Tian, Q., Wang, M.: Swin-unet: Unet-like pure transformer for medical image segmentation. In: European conference on computer vision. pp. 205–218. Springer (2022)
4. Carion, N., Massa, F., Synnaeve, G., Usunier, N., Kirillov, A., Zagoruyko, S.: End-to-end object detection with transformers. In: European conference on computer vision. pp. 213–229. Springer (2020)
5. Chen, H., Wang, Y., Guo, T., Xu, C., Deng, Y., Liu, Z., Ma, S., Xu, C., Xu, C., Gao, W.: Pre-trained image processing transformer. In: Proceedings of the IEEE/CVF conference on computer vision and pattern recognition. pp. 12299–12310 (2021)
6. Chen, X., Wang, X., Zhou, J., Qiao, Y., Dong, C.: Activating more pixels in image super-resolution transformer. In: Proceedings of the IEEE/CVF conference on computer vision and pattern recognition. pp. 22367–22377 (2023)
7. Choi, H., Lee, J., Yang, J.: N-gram in swin transformers for efficient lightweight image super-resolution. In: Proceedings of the IEEE/CVF Conference on Computer Vision and Pattern Recognition. pp. 2071–2081 (2023)
8. Chu, X., Zhang, B., Ma, H., Xu, R., Li, Q.: Fast, accurate and lightweight super-resolution with neural architecture search. In: 2020 25th International conference on pattern recognition (ICPR). pp. 59–64. IEEE (2021)
9. Dai, T., Cai, J., Zhang, Y., Xia, S.T., Zhang, L.: Second-order attention network for single image super-resolution. In: Proceedings of the IEEE/CVF conference on computer vision and pattern recognition. pp. 11065–11074 (2019)
10. Dong, C., Loy, C.C., He, K., Tang, X.: Image super-resolution using deep convolutional networks. *IEEE transactions on pattern analysis and machine intelligence* **38**(2), 295–307 (2015)
11. Gao, Q., Zhao, Y., Li, G., Tong, T.: Image super-resolution using knowledge distillation. In: Asian Conference on Computer Vision. pp. 527–541. Springer (2018)
12. Goodfellow, I., Pouget-Abadie, J., Mirza, M., Xu, B., Warde-Farley, D., Ozair, S., Courville, A., Bengio, Y.: Generative adversarial nets. *Advances in neural information processing systems* **27** (2014)
13. Huang, J.B., Singh, A., Ahuja, N.: Single image super-resolution from transformed self-exemplars. In: Proceedings of the IEEE conference on computer vision and pattern recognition. pp. 5197–5206 (2015)
14. Hui, Z., Gao, X., Yang, Y., Wang, X.: Lightweight image super-resolution with information multi-distillation network. In: Proceedings of the 27th acm international conference on multimedia. pp. 2024–2032 (2019)
15. Kim, J., Lee, J.K., Lee, K.M.: Accurate image super-resolution using very deep convolutional networks. In: Proceedings of the IEEE conference on computer vision and pattern recognition. pp. 1646–1654 (2016)
16. Kim, J., Lee, J.K., Lee, K.M.: Deeply-recursive convolutional network for image super-resolution. In: Proceedings of the IEEE conference on computer vision and pattern recognition. pp. 1637–1645 (2016)

17. Kong, F., Li, M., Liu, S., Liu, D., He, J., Bai, Y., Chen, F., Fu, L.: Residual local feature network for efficient super-resolution. In: Proceedings of the IEEE/CVF Conference on Computer Vision and Pattern Recognition. pp. 766–776 (2022)
18. Ledig, C., Theis, L., Huszár, F., Caballero, J., Cunningham, A., Acosta, A., Aitken, A., Tejani, A., Totz, J., Wang, Z., et al.: Photo-realistic single image super-resolution using a generative adversarial network. In: Proceedings of the IEEE conference on computer vision and pattern recognition. pp. 4681–4690 (2017)
19. Li, X., Wang, W., Hu, X., Yang, J.: Selective kernel networks. In: Proceedings of the IEEE/CVF conference on computer vision and pattern recognition. pp. 510–519 (2019)
20. Liang, J., Cao, J., Sun, G., Zhang, K., Van Gool, L., Timofte, R.: Swinir: Image restoration using swin transformer. In: Proceedings of the IEEE/CVF international conference on computer vision. pp. 1833–1844 (2021)
21. Lim, B., Son, S., Kim, H., Nah, S., Mu Lee, K.: Enhanced deep residual networks for single image super-resolution. In: Proceedings of the IEEE conference on computer vision and pattern recognition workshops. pp. 136–144 (2017)
22. Liu, C., Yang, H., Fu, J., Qian, X.: Learning trajectory-aware transformer for video super-resolution. In: Proceedings of the IEEE/CVF Conference on Computer Vision and Pattern Recognition. pp. 5687–5696 (2022)
23. Liu, J., Tang, J., Wu, G.: Residual feature distillation network for lightweight image super-resolution. In: Computer Vision–ECCV 2020 Workshops: Glasgow, UK, August 23–28, 2020, Proceedings, Part III 16. pp. 41–55. Springer (2020)
24. Lu, Z., Li, J., Liu, H., Huang, C., Zhang, L., Zeng, T.: Transformer for single image super-resolution. In: Proceedings of the IEEE/CVF conference on computer vision and pattern recognition. pp. 457–466 (2022)
25. Luo, X., Xie, Y., Zhang, Y., Qu, Y., Li, C., Fu, Y.: Latticenet: Towards lightweight image super-resolution with lattice block. In: Computer Vision–ECCV 2020: 16th European Conference, Glasgow, UK, August 23–28, 2020, Proceedings, Part XXII 16. pp. 272–289. Springer (2020)
26. Martin, D., Fowlkes, C., Tal, D., Malik, J.: A database of human segmented natural images and its application to evaluating segmentation algorithms and measuring ecological statistics. In: Proceedings Eighth IEEE International Conference on Computer Vision. ICCV 2001. vol. 2, pp. 416–423. IEEE (2001)
27. Matsui, Y., Ito, K., Aramaki, Y., Fujimoto, A., Ogawa, T., Yamasaki, T., Aizawa, K.: Sketch-based manga retrieval using manga109 dataset. *Multimedia Tools and Applications* **76**, 21811–21838 (2017)
28. Mei, Y., Fan, Y., Zhou, Y.: Image super-resolution with non-local sparse attention. In: Proceedings of the IEEE/CVF Conference on Computer Vision and Pattern Recognition. pp. 3517–3526 (2021)
29. Niu, B., Wen, W., Ren, W., Zhang, X., Yang, L., Wang, S., Zhang, K., Cao, X., Shen, H.: Single image super-resolution via a holistic attention network. In: Computer Vision–ECCV 2020: 16th European Conference, Glasgow, UK, August 23–28, 2020, Proceedings, Part XII 16. pp. 191–207. Springer (2020)
30. Park, S.H., Moon, Y.S., Cho, N.I.: Flexible style image super-resolution using conditional objective. *IEEE Access* **10**, 9774–9792 (2022)
31. Park, S.H., Moon, Y.S., Cho, N.I.: Perception-oriented single image super-resolution using optimal objective estimation. In: Proceedings of the IEEE/CVF Conference on Computer Vision and Pattern Recognition. pp. 1725–1735 (2023)
32. Pramanick, A., Megha, D., Sur, A.: Attention-based spatial-frequency information network for underwater single image super-resolution. In: ICASSP 2024-2024 IEEE

- International Conference on Acoustics, Speech and Signal Processing (ICASSP). pp. 3560–3564. IEEE (2024)
33. Rakotonirina, N.C., Rasoanaivo, A.: Esrgan+: Further improving enhanced super-resolution generative adversarial network. In: ICASSP 2020-2020 IEEE International Conference on Acoustics, Speech and Signal Processing (ICASSP). pp. 3637–3641. IEEE (2020)
 34. Tai, Y., Yang, J., Liu, X.: Image super-resolution via deep recursive residual network. In: Proceedings of the IEEE conference on computer vision and pattern recognition. pp. 3147–3155 (2017)
 35. Tai, Y., Yang, J., Liu, X., Xu, C.: Memnet: A persistent memory network for image restoration. In: Proceedings of the IEEE international conference on computer vision. pp. 4539–4547 (2017)
 36. Timofte, R., Agustsson, E., Van Gool, L., Yang, M.H., Zhang, L.: Ntire 2017 challenge on single image super-resolution: Methods and results. In: Proceedings of the IEEE conference on computer vision and pattern recognition workshops. pp. 114–125 (2017)
 37. Wang, H., Chen, X., Ni, B., Liu, Y., Liu, J.: Omni aggregation networks for lightweight image super-resolution. In: Proceedings of the IEEE/CVF Conference on Computer Vision and Pattern Recognition. pp. 22378–22387 (2023)
 38. Wang, X., Yu, K., Wu, S., Gu, J., Liu, Y., Dong, C., Qiao, Y., Change Loy, C.: Esrgan: Enhanced super-resolution generative adversarial networks. In: Proceedings of the European conference on computer vision (ECCV) workshops. pp. 0–0 (2018)
 39. Wang, Z., Cun, X., Bao, J., Zhou, W., Liu, J., Li, H.: Uformer: A general u-shaped transformer for image restoration. In: Proceedings of the IEEE/CVF conference on computer vision and pattern recognition. pp. 17683–17693 (2022)
 40. Wu, B., Xu, C., Dai, X., Wan, A., Zhang, P., Yan, Z., Tomizuka, M., Gonzalez, J., Keutzer, K., Vajda, P.: Visual transformers: Token-based image representation and processing for computer vision. arXiv preprint arXiv:2006.03677 (2020)
 41. Zamir, S.W., Arora, A., Khan, S., Hayat, M., Khan, F.S., Yang, M.H.: Restormer: Efficient transformer for high-resolution image restoration. In: Proceedings of the IEEE/CVF conference on computer vision and pattern recognition. pp. 5728–5739 (2022)
 42. Zeyde, R., Elad, M., Protter, M.: On single image scale-up using sparse-representations. In: Curves and Surfaces: 7th International Conference, Avignon, France, June 24-30, 2010, Revised Selected Papers 7. pp. 711–730. Springer (2012)
 43. Zhang, D., Huang, F., Liu, S., Wang, X., Jin, Z.: Swinfir: Revisiting the swinir with fast fourier convolution and improved training for image super-resolution. arXiv preprint arXiv:2208.11247 (2022)
 44. Zhang, K., Zuo, W., Zhang, L.: Learning a single convolutional super-resolution network for multiple degradations. In: Proceedings of the IEEE conference on computer vision and pattern recognition. pp. 3262–3271 (2018)
 45. Zhang, X., Zeng, H., Guo, S., Zhang, L.: Efficient long-range attention network for image super-resolution. In: European Conference on Computer Vision. pp. 649–667. Springer (2022)
 46. Zhang, Y., Chen, H., Chen, X., Deng, Y., Xu, C., Wang, Y.: Data-free knowledge distillation for image super-resolution. In: Proceedings of the IEEE/CVF Conference on Computer Vision and Pattern Recognition. pp. 7852–7861 (2021)
 47. Zhang, Y., Li, K., Li, K., Wang, L., Zhong, B., Fu, Y.: Image super-resolution using very deep residual channel attention networks. In: Proceedings of the European conference on computer vision (ECCV). pp. 286–301 (2018)